

Conjugated Polymer Superlattices for Enhanced Charge Transport in Organic Solar Cells

Undergraduate Thesis

Karthik Iyengar Seetharam

Advisor: Assistant Professor Adrienne D. Stiff-Roberts

Department of Electrical and Computer Engineering

Duke University

Table of Contents

Abstract	2
Introduction	3
Computational Model	4
Calculation of Forward Bias Transmission Coefficient.....	4
Calculation of the Dark Current Density	6
Calculation of the Photocurrent Density	6
Calculation of the Total Current.....	7
List of Assumptions	7
Model Results	8
Model Discussion	14
Experimental Work	16
Experimental Work Discussion	18
Future Investigation	19
Conclusions	19
Acknowledgements.....	19
References	20

Abstract

Commercially available silicon-based inorganic photovoltaic (IPV) cells currently have a conversion efficiency of approximately 10-20% with a theoretical limit at 31% for Si devices. Other IPVs based on compound semiconductors have achieved efficiencies up to 41% using multi-layer tandem structures, but have not penetrated the terrestrial market due to the prohibitive cost of mass production. Organic materials offer an exciting economical alternative because of their flexibility and low manufacturing cost. Since organic photovoltaics (OPVs) are much cheaper to fabricate, improving OPV efficiency might provide an economical and sustainable solution for growing energy demand. This study aims to design and to build an efficient OPV using a polymer superlattice nanostructure that improves charge transport via miniband formation. A superlattice model based on elementary solid state physics was developed to understand and predict the current-voltage (IV) behavior of a polymer superlattice. The model predicts that it is possible to significantly enhance power output in a superlattice OPV from resonant tunneling as compared to a standard bulk heterojunction OPV. A prototype device was built based on physical insight on thickness, crystallinity, and interface roughness gained through modeling. A PPy and P3HT conjugated polymer superlattice (~3nm/layer) was spin-cast on a Si substrate with Au and Al contacts for holes and electrons, respectively, and characterized by Atomic Force Microscopy and Spectroscopic Ellipsometry. Results show that it is possible to fabricate ultrathin (<10nm) sub-nm surface roughness polymer films. However, negative differential resistance in the IV curves was not seen. The crystallinity and interface properties of ultrathin multilayer polymer films are current topics of investigation.

Introduction

The Energy Information Administration (EIA) projects that world energy consumption will increase 49% by 2035¹. Fossil fuels will not be able to keep up with rising demands forever. Solar energy is abundant, free, and if harvested right, can serve as a sustainable source of energy. In addition, solar energy is environmentally friendly producing little to none chemical or radioactive byproducts compared to fossil fuel based or nuclear energy plants. However, solar energy comprises only 1 percent of the total energy market due to its limited economic viability¹. If solar energy from current photovoltaic cells (PV) or concentrated solar power (CSP) is integrated into the power grid, it would cost up to 6 times the price of energy produced from fossil fuels.² Due to increased research and development funding from the DOE's Solar Energy Technology Program, the PV market is projected to increase from 480MW of grid-connected power at the end of 2006 to 24GW by 2015. Similarly an increase of 25GW is expected in the CSP market.³

According to the National Academy of Engineering, the technological challenges that limit the economic viability of current solar technology are solar conversion efficiency and the energy storage for use during poor visibility hours. Commercially available silicon-based inorganic photovoltaic (IPV) cells currently have a conversion efficiency of approximately 10-20% with a theoretical limit at 31% for Si devices.² Other IPVs based on compound semiconductors such as Gallium-Arsenide (GaAs) have achieved efficiencies up to 40.8% using multi-layer tandem structures⁴, but because of the prohibitive cost of mass producing compound semiconductors, have not penetrated the terrestrial market.

Thus, PV research has taken a new direction in exploring the uses of different materials for the construction of flexible and more efficient solar cells that might offer a viable economical solution to the solar energy challenges. Organic materials offer an exciting alternative because of their low manufacturing cost and as such have gained considerable interest as a potential bulk material for PV devices.

However, the challenges associated with organic photovoltaics (OPV) are widespread. A key difference between IPVs and OPVs is the photogeneration of charge. In IPVs, light absorption in the active layer produces free electron-hole pairs that are separated by the built-in electric field such that they can be collected at the contacts as a current. However, in OPVs, light absorption generates excitons, tightly bound mobile charged states. Excitons must be further dissociate at a donor-acceptor interface in the absence of a built-in electric field to produce electrons and holes before being transported to the contacts.⁵ Hence, the only mode of charge transport in OPVs for excitons and electron-hole pairs is diffusion compared to drift and diffusion present in IPVs. In addition, the diffusion length of excitons in the bulk -- about 15 nm -- is much shorter than that of electrons and holes in doped Si, and hence provides further difficulty in dissociating excitons.⁶ In order to create charge carriers, exciton dissociation must take place at a donor-acceptor (D-A) interface and hence an acceptor species must be present within the short diffusion length.

The external quantum efficiency (EQE) is a figure of merit for a PV. The EQE measures the efficiency in converting individual photons to current as a function of wavelength. The four main factors that contribute to the EQE are, the photon conversion efficiency (exciton generation), the exciton diffusion (to a D-A interface) efficiency, the charge transfer (exciton dissociation) efficiency, and the charge transport (collection) efficiency.⁶ The EQE is closely related to the power conversion efficiency (PCE) which is the ratio of the input and output powers summed over all wavelengths.⁷ To date, the highest PCE achieved with an OPV is

approximately 6% with a bulk heterojunction (BHJ) mixture of fullerene derivatives (PCBM) and conjugated polymers (P3HT).⁸ In order to significantly increase the PCE, one must optimize the materials selection, control the material morphology, and optimize device structure.

The goal of this research is to enhance the charge transfer and dissociation efficiency of an OPV by introducing a superlattice nanostructure. A planar superlattice structure is made from alternating ultrathin (<10nm) layers of two materials with different energy band offsets. With enough periodicity in the superlattice, energy minibands form as a result of quantum mechanics. Minibands are ranges of energies where there are many closely packed (energetically) bound states that act as continuous energy band where delocalization of the charge carrier wavefunctions occurs. Due to the increased tunneling probabilities, charge carriers that transition into these minibands can reach the contacts with higher probability. In solid state superlattices, this phenomenon is observed in a current voltage measurement where, over a certain region of applied bias, the total current is amplified due to the presence of strong tunneling.⁹ Superlattice nanostructures in organic materials have, to the author's best knowledge, not been physically demonstrated. An organic superlattice PV might potentially yield a larger net power from the amplified tunneling current compared to a BHJ PV.

Computational Model

Calculation of Forward Bias Transmission Coefficient

The 1D time-independent coordinate-space Schrodinger Equation for a linear potential from a constant electric field is given in Equation 1. Making the change variable shown in Equation 2, the Schrodinger Equation can be expressed as the Airy differential equation (Equation 3) in ρ . The wavefunction solutions in each region of the linear potential are then a superposition of Airy functions of the first and second kind. The Transfer Matrix Method (TMM) matches the wavefunction solutions at each heterojunction interface as required by the quantum mechanical boundary conditions (Equation 4).

Equation 1:

$$-\frac{\hbar^2}{2m} \frac{d^2\psi}{dz_i^2} + (U_{pot,i} - eF_i z_i)\psi = E\psi$$

Equation 2:

$$\rho_i = \left(\frac{2m_i}{F_i^2 e^2 \hbar^2}\right)^{1/3} (-eF_i z_i - E - U_{pot,i}), \quad \gamma_i = -\frac{d\rho_i}{dz_i}$$

Equation 3:

$$\frac{d^2\psi_i}{d\rho_i^2} = \rho_i \psi_i$$

Equation 4:

$$\psi_i = \psi_{i+1}$$

$$\frac{\gamma_i}{m_i} \frac{d\psi_i}{dz_i} = \frac{\gamma_{i+1}}{m_{i+1}} \frac{d\psi_{i+1}}{dz_i}$$

Where F_i is the applied field in region i , $U_{pot,i}$ is the potential in region i , e is the electric charge, and m_i is the effective mass in region i .

The solution in the first region, the hole contact with $V=0$, is a superposition of forward (incoming) moving and backward (reflected) moving plane waves of the incident electron. Matching the solutions between region 1 and region 2, the first polymer layer, we obtain Equation 5.

Equation 5:

$$M_1 = \frac{1}{2} \begin{bmatrix} (Ai(\rho_1) + i\eta Ai'(\rho_1))\exp(-ik_0 z_1) & (Bi(\rho_1) + i\eta Bi'(\rho_1))\exp(-ik_0 z_1) \\ (Ai(\rho_1) - i\eta Ai'(\rho_1))\exp(ik_0 z_1) & (Bi(\rho_1) - i\eta Bi'(\rho_1))\exp(ik_0 z_1) \end{bmatrix}, \eta = \frac{m_0 \gamma_1}{m_1 k_0}$$

Similarly, the last region, region N , is the electron contact and hence $V=0$. We must match the Airy solutions of region $N-1$, the last polymer layer, and the plane wave solution of region N . Region N only allows a forward moving plane wave solution as we are only concerned with forward transmission of the incident electron (the backward moving wave is thrown out on physical grounds). The matrix representation is given Equation 6.

Equation 6:

$$M_N = \pi \begin{bmatrix} (Bi'(\rho_{N-1}) + i\xi Bi(\rho_{N-1}))\exp(ik_N z_N) & 0 \\ -(Ai'(\rho_{N-1}) + i\xi Ai(\rho_{N-1}))\exp(ik_N z_N) & 0 \end{bmatrix}, \xi = \frac{k_N m_{N-1}}{m_N \gamma_{N-1}}$$

In the active layer of the superlattice which contains polymer-polymer interfaces, we match the Airy solutions in region i to the Airy solutions in region $i + 1$. The matrix representation is shown in Equation 7.

Equation 7:

$$M_i = \pi \begin{bmatrix} (Ai(\rho_{i+1})Bi'(\rho_i) - \sigma Ai'(\rho_{i+1})Bi(\rho_i)) & (Bi(\rho_{i+1})Bi'(\rho_i) - \sigma Bi'(\rho_{i+1})Bi(\rho_i)) \\ (\sigma Ai'(\rho_{i+1})Ai(\rho_i) - Ai(\rho_{i+1})Ai'(\rho_i)) & (\sigma Bi'(\rho_{i+1})Ai'(\rho_i) - Bi(\rho_{i+1})Ai'(\rho_i)) \end{bmatrix}$$

$$\sigma = \frac{m_i \gamma_{i+1}}{m_{i+1} \gamma_i}$$

Finally, the individual transfer matrices are multiplied together to form the overall the transfer matrix for the whole structure (Equation 8). Acting W on the incident electron probability amplitudes, we calculate the square of the ratio of the final probability amplitude of the transmitted wave to the probability amplitude of the incident forward moving wave. Converting the ratio of probability amplitudes to a ratio of probability current densities, we finally reach Equation 9, the forward bias transmission coefficient for the whole structure. This derivation is based on Vatannia 1996¹⁰.

Equation 8:

$$W = \prod_{i=1}^N M_i$$

Equation 9:

$$D(E) = \frac{k_N m_0}{k_0 m_N} \frac{1}{|W_{11}|^2}$$

Calculation of the Dark Current Density

The dark current density is calculated using a standard result from solid state physics for a metal-active region-metal structure where the active region has a transmission coefficient $D(E)$ (Equation 10). This result assumes the metal contacts are free electron gases. See Fromhold¹¹ for details on the derivation.

Equation 10:

$$J_{dark}(V) = \frac{emkT}{2\pi^2 \hbar^3} \int_0^\infty D(E, V) \ln\left(\frac{1 + \exp((E_{f1} - E)/kT)}{1 + \exp((E_{f2} - E - eV_a)/kT)}\right) dE$$

Where V_a is the applied bias, E_{f1} is the Fermi energy of the first contact at temperature T relative to its Fermi energy at 0K, E_{f2} is the Fermi energy in the second contact at temperature T relative to its Fermi energy at 0K, and k is the Boltzmann constant.

Calculation of the Photocurrent Density

We assume a simple carrier generation process as follows: An AM1.5 Direct Sunlight incident spectrum is converted into a photon flux as a function of energy $N_0(E)$. Assuming an exciton generation efficiency η_1 , exciton diffusion efficiency η_2 , and exciton dissociation efficiency η_3 , we calculate the number of free charges generated via absorption across the smallest HOMO-

LUMO gap of the donor and acceptor layers by Equation 11. We assume the free charges see the same transmission coefficient everywhere in the structure (See List of Assumptions).

Equation 11:

$$N(E) = \eta_1 \eta_2 \eta_3 N_0(E) \text{ for } E \geq \min(E_{g,donor}, E_{g,acceptor})$$

Hence, the photocurrent is given by Equation 12.

Equation 12:

$$J_{photo}(V) = e \int_0^{\infty} D(E, V) N(E) dE$$

Calculation of the Total Current

The total current in the organic superlattice photovoltaic is given by Equation 13. The negative sign of the photocurrent appears since the photocurrent flows in the opposite direction of the dark current due to the difference in the work functions of the metal contacts – the effect is similar to that of the built-in electric field in a semiconductor PN junction¹².

Equation 13:

$$J_{total}(V) = J_{dark}(V) - J_{photo}(V)$$

List of Assumptions

- Assume only 1 way forward transitions in transmission coefficient calculation
- Neglect space charge effects from carrier buildup (ignore band-bending)
- Assume carrier sees same transmission coefficient at any point in the structure
- Ignore level filling from carrier generation
- Ignore coupling (selection rules) from photons to electron-hole pairs/excitons
- All carriers generated in the smallest band gap material
- Only considering free carrier species in charge transport
- Assume coherent transport – wavefunction extends from contact 1 to contact 2
- Losses due to recombination, absorption inefficiencies, dissociation inefficiencies are all encompassed in numerical factors that decrease photocurrent
- Assume only interband transitions for carrier generation

- Assume same order of magnitude for photocurrent and dark current (scaled to values in Forrest 2010¹²)
- Neglect frequency dependence of dielectric constant over incident spectrum range
- Assume values of effective mass (sensitive parameter with no literature values for organic materials)

Model Results

A poly(2-methoxy-5-(3',7'-dimethyl-octyloxy))-p-phenylene vinylene, (MDMO-PPV):poly(3-hexylthiophene) (P3HT) superlattice with 4 periods was simulated. The electron conduction band diagram is shown in Figure 1 where A is the LUMO of MDMO-PPV, B is the LUMO of P3HT, and C_e is the Fermi level of the Al electron contact. The superlattice has a type II band lineup where the Fermi level of the ITO/glass hole contact C_h is 0.4eV below C_e , the HOMO of MDMO-PPV is 0.3eV below C_h , and the HOMO of P3HT is 0.4eV below the HOMO of MDMO-PPV (valence band diagram not shown).

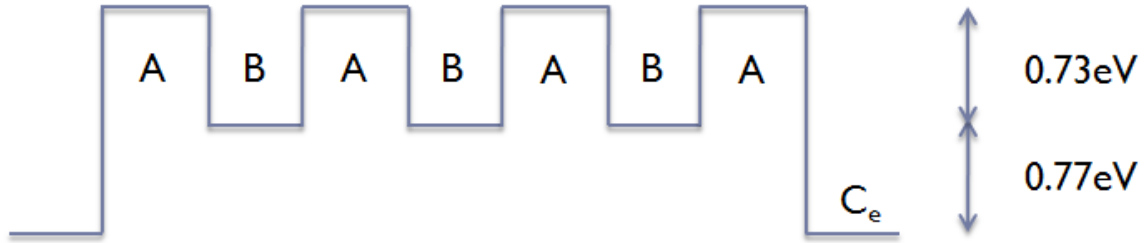


Figure 1: Electron conduction band lineup for MDMO-PPV:P3HT cell.

The results were calculated for 1nm layers of donors and acceptors with $m_{\text{well}}=0.42$, $m_{\text{barrier}}=0.05$, $\epsilon_{\text{well}}=1.7$, $\epsilon_{\text{barrier}}=1.9$, $T=300\text{K}$, $E_{f1}=E_{f2}=0.005\text{eV}$ (as measured from metal conduction band edge). All efficiencies were assumed to be 1 such that photon to electron conversion is ideal.

Figure 2 shows the incident AM1.5 solar spectrum and corresponding energy spectrum of the free carriers created from absorption. Figure 3 shows the forward bias transmission coefficient as a function of energy and applied bias for the superlattice structure. Figure 4 shows the calculated dark current and Figure 5 shows the calculated photocurrent. Figure 6 shows the total electron and hole currents. Finally, the total $J(V)$ for the whole device is shown in Figure 7 and compared to a representative $J(V)$ curve from a standard BHJ bilayer cell.¹²

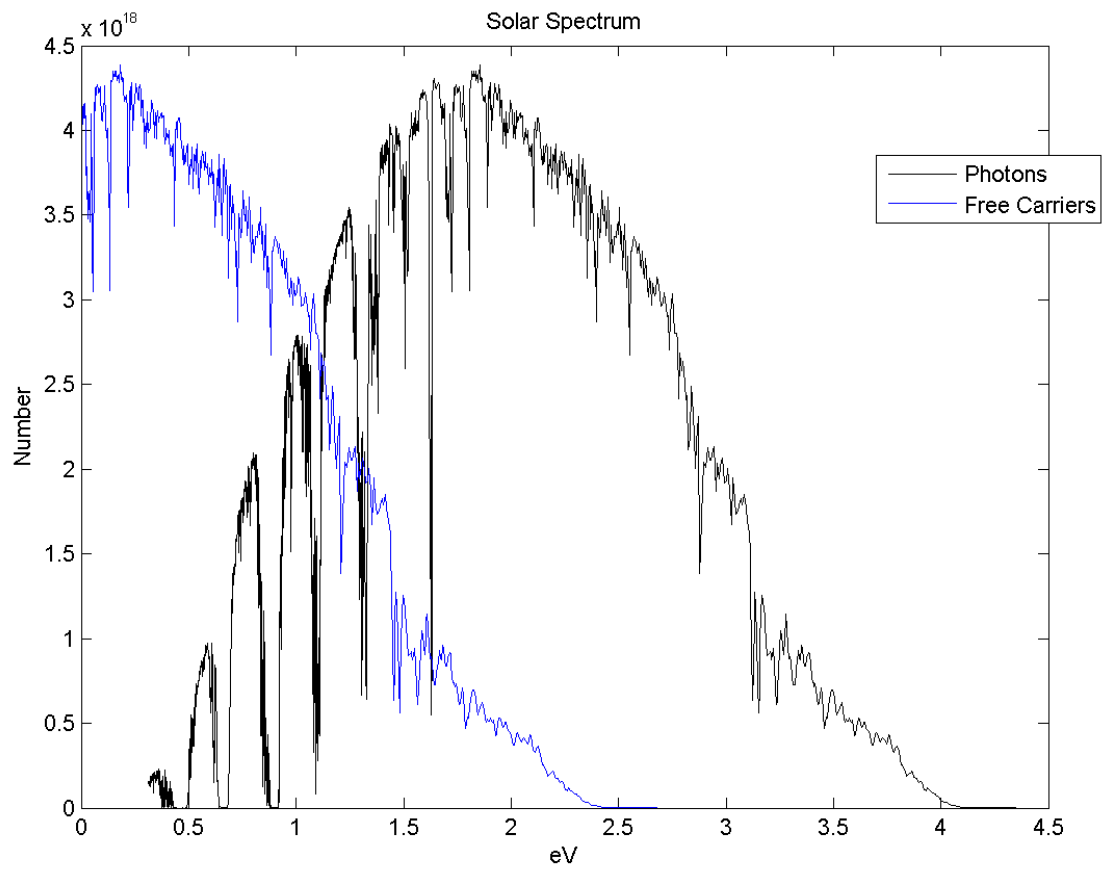


Figure 2: Incident AM1.5 Solar spectrum and energy spectrum of free carriers generated by absorption

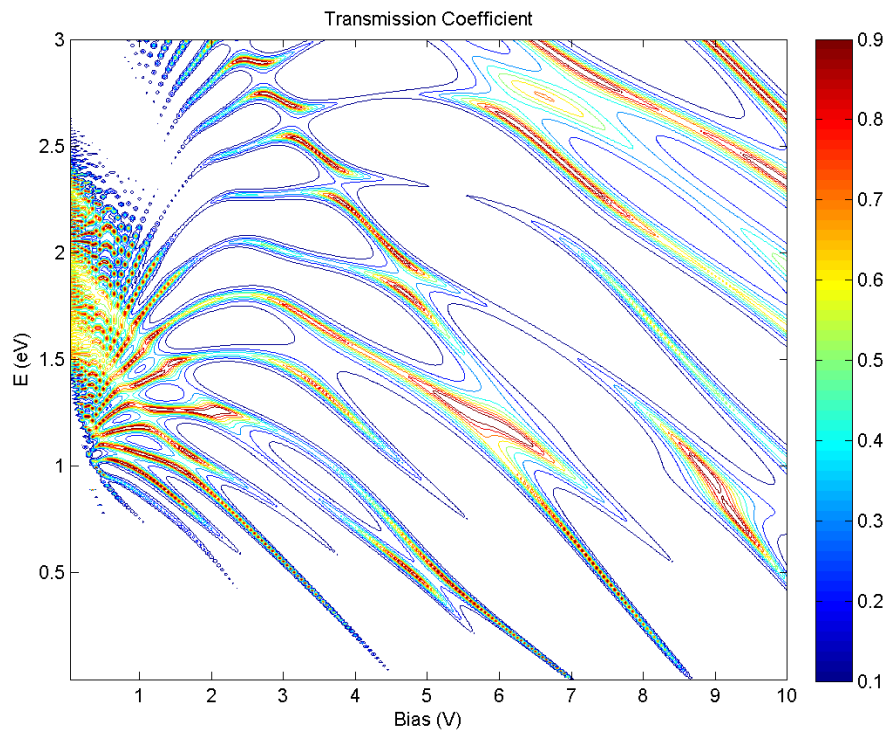


Figure 3a: Electron transmission coefficient of MDMO-PPV:P3HT superlattice structure

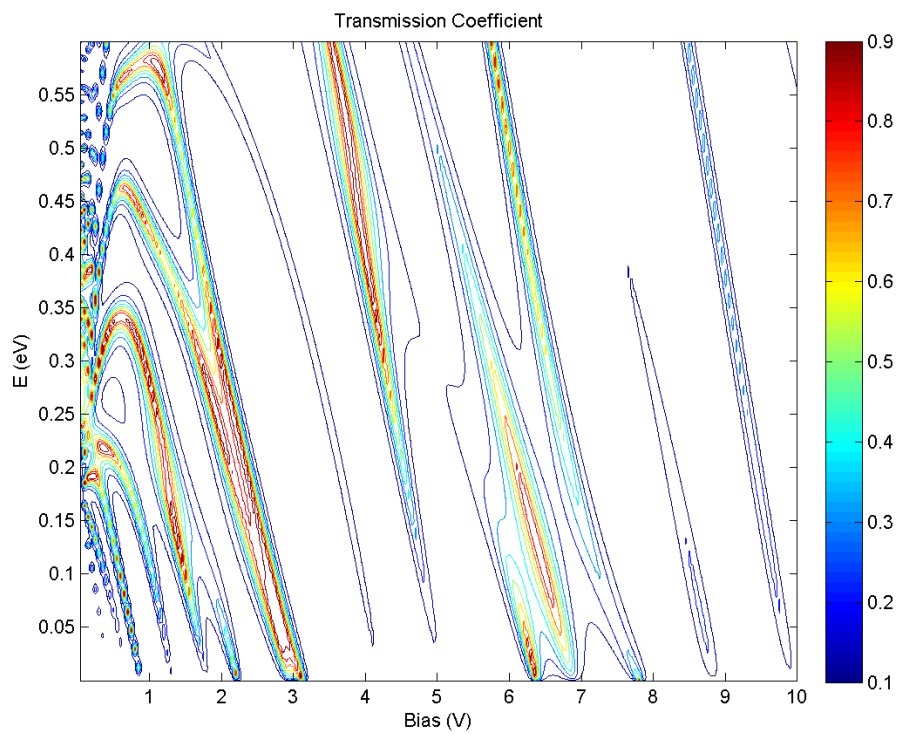


Figure 3b: Hole transmission coefficient of MDMO-PPV:P3HT superlattice structure (positive E in this figure indicates increasing energy away (more negative) from the valence band edge).

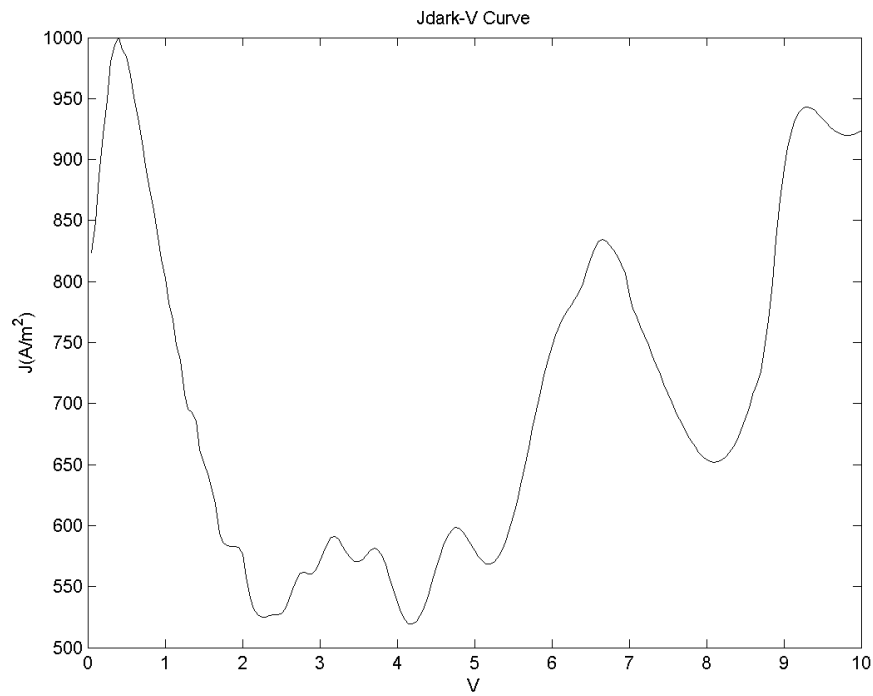


Figure 4a: Electron dark current for MDMO-PPV:P3HT superlattice

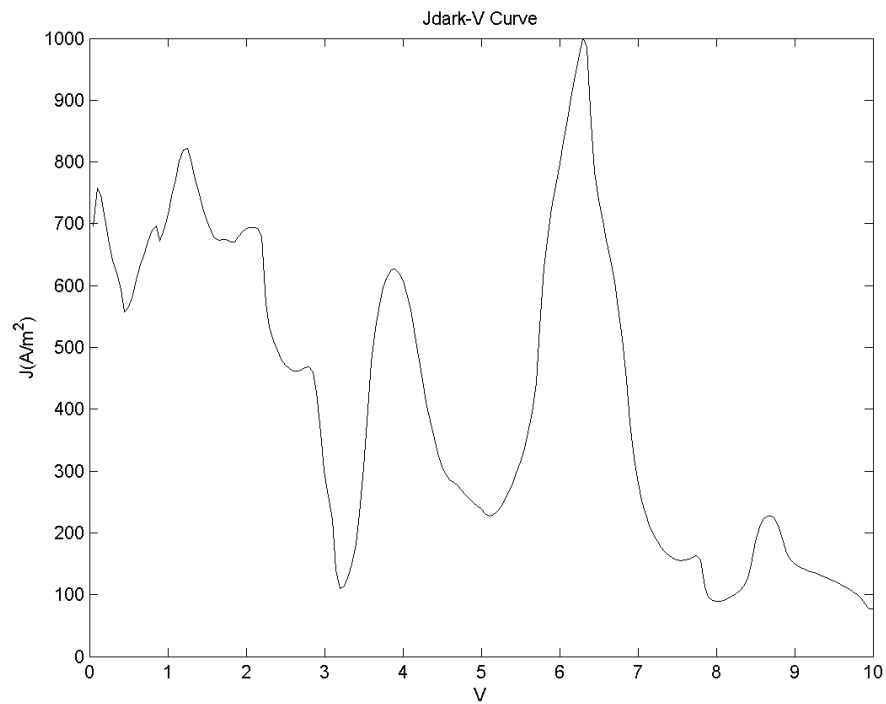


Figure 4b: Hole dark current for MDMO-PPV:P3HT superlattice

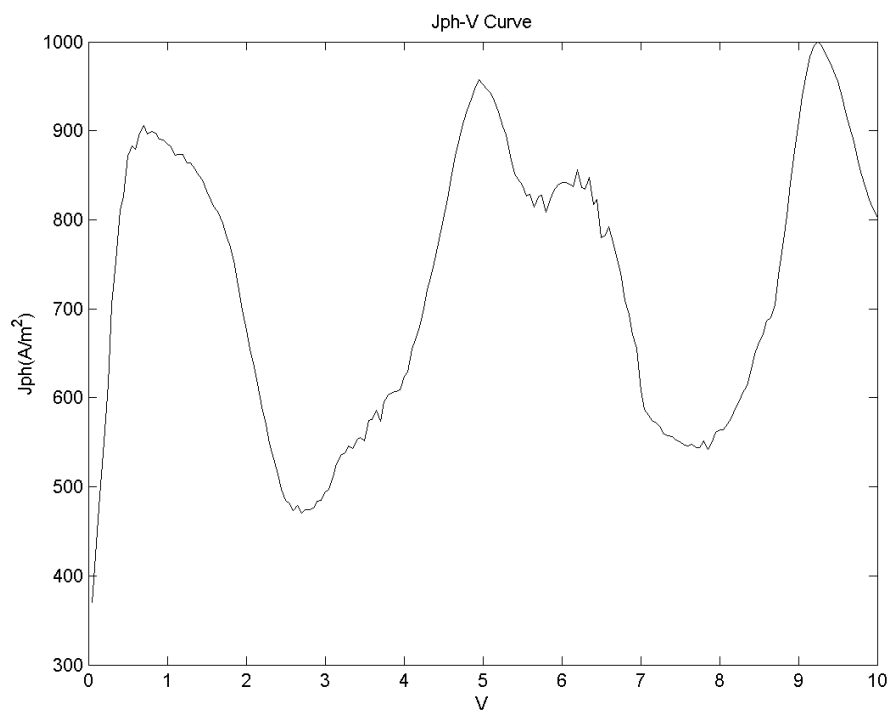


Figure 5a: Electron photocurrent for MDMO-PPV:P3HT superlattice

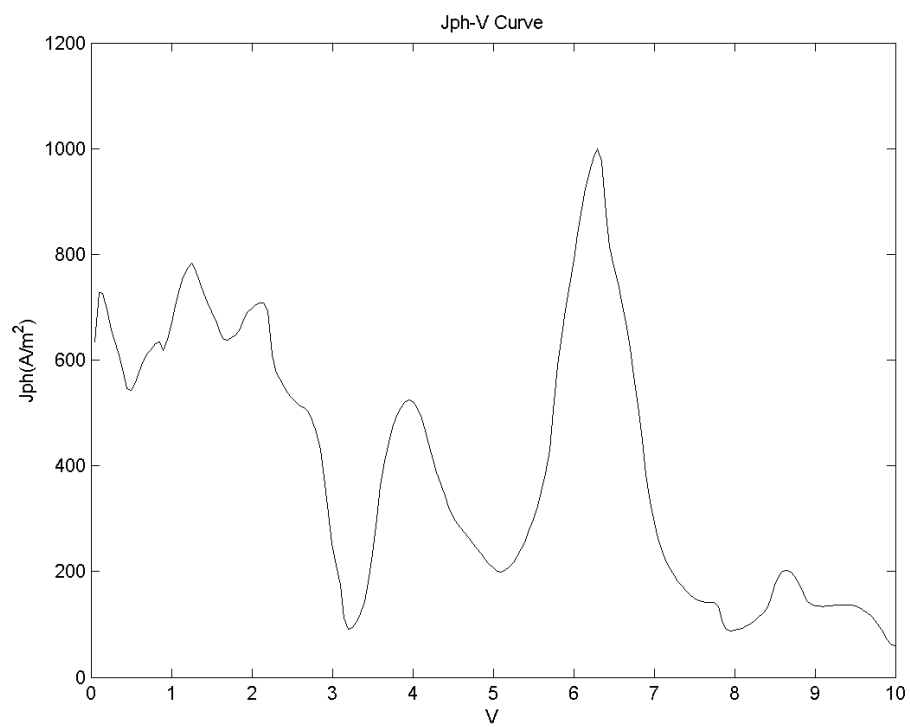


Figure 5b: Hole photocurrent for MDMO-PPV:P3HT superlattice

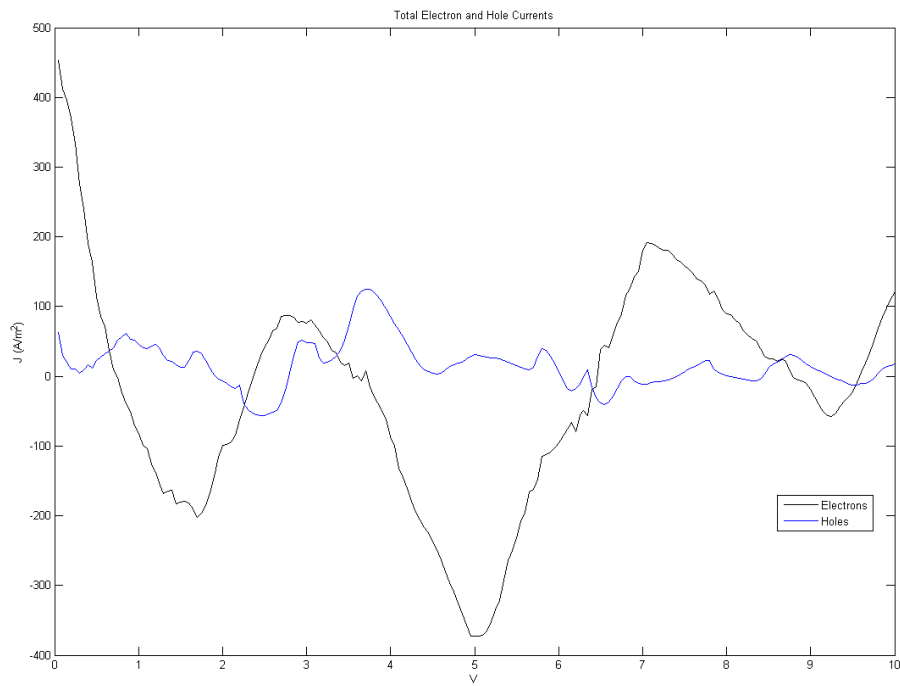


Figure 6: Total Electron and Hole Currents for MDMO-PPV:P3HT superlattice

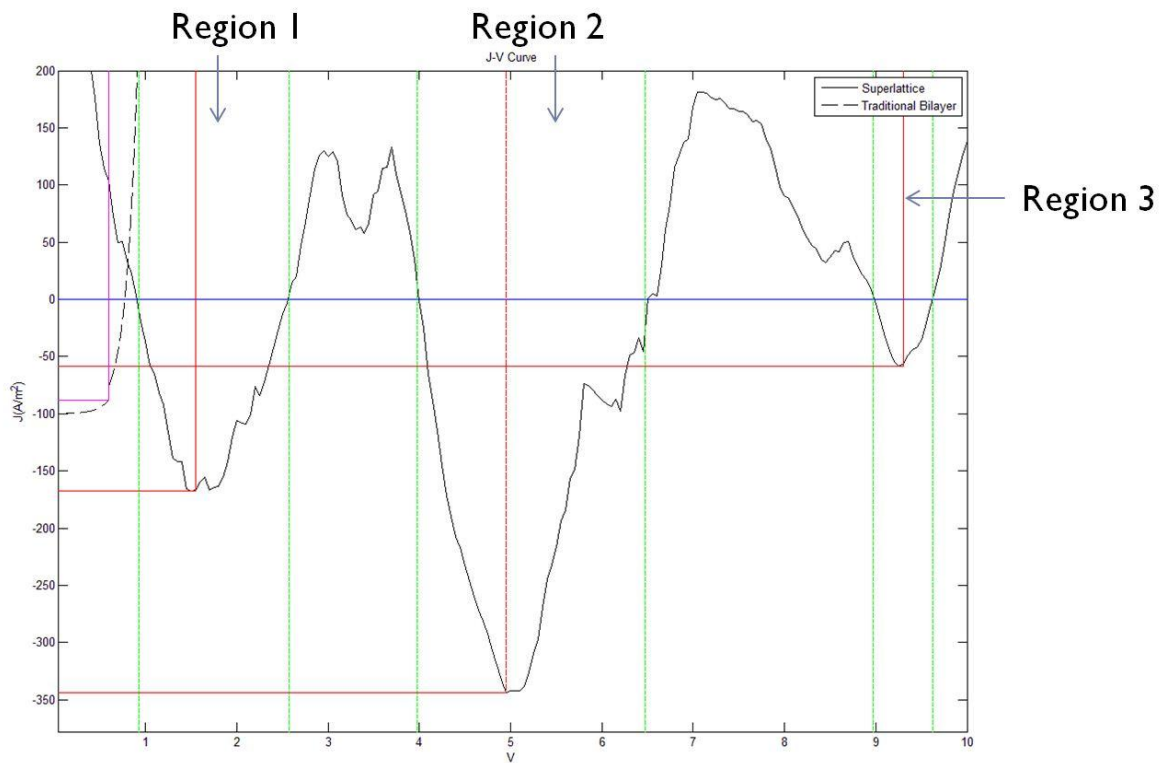


Figure 7: Total current for MDMO-PPV:P3HT superlattice compared to traditional bilayer cell

Model Discussion

In Figure 7, we see that the superlattice nanostructure can significantly improve the total power output of an OPV. Compared to the traditional bilayer BHJ cell, which suggests a 1 V optimal power point, the superlattice structure, due to resonant tunneling, suggests an optimal power point of 5 V with a significantly larger current density of approximately -350 A/m^2 . In practice, devices are limited by the open circuit voltage (V_{oc}) which is usually less than 5 V. Even if it were possible to match a load corresponding to 5 V, morphological degradation in the active layer will likely occur. A combination of parameters that yields large resonance peaks around practical values of around 1 V might exist. Furthermore, there are multiple operating regions for the superlattice device, all of which lead to higher power outputs than a traditional bilayer device. The ratio of optimal superlattice power output to optimal bilayer power output in each operating region is 4.94, 32.39, and 10.38 for regions 1, 2, and 3 respectively. This suggests that a superlattice device effectively has multiple “traditional” V_{oc} points that mark the boundaries of the operating regions (the green lines in Figure 7) although for any practical device, there is only one true performance limiting V_{oc} .

From Figure 3a, the electron transmission coefficient shows large magnitude transmission (>0.9) for the bound states ($<1.5\text{eV}$) in the conduction band. Similarly, Figure 3b shows large magnitude transmission for the bound states ($<0.3\text{eV}$) in the valence band. This is due to the miniband formation as bound state energy levels align at various bias ranges and as such allow tunneling of electrons/holes between layers. Strong minibands are also noted at continuum energies above the conduction and below the valence band edges from energetic proximity to the superlattice.

In Figure 4, we see the resonant tunneling characteristics of a superlattice with regions of peaked electron and hole dark currents due to miniband formation. From Figure 5a, the electron photocurrent also has large peaks in the current, although the locations of the peaks differ from those of the electron dark current. However, from Figure 5b, the locations of the peaks for the hole photocurrent and hole dark current are approximately the same. The total hole current is several times smaller than the total electron current (Figure 6) and hence the total current in the device is dominated by electron transport. The mismatched overlap of the peaks in the electron dark current and electron photocurrent leads to an interesting total current with large negative peaks; the enhanced 4th quadrant current leads to increased power output from a photovoltaic device. Thus, under several assumptions, the model demonstrates the advantage of using a superlattice nanostructure in an OPV.

From Figure 2, we can see that approximately half of the incident spectrum is absorbed given the large HOMO-LUMO gaps of most conjugated polymer materials. The HOMO-LUMO gap is a

function of the inherent polymer chemistry and the chain packing resultant from the particular fabrication technique used. Since the orientation and packing of the polymer chains is sensitive to the fabrication technique, it is hard to pin down the conjugation lengths that lead to the “crystalline” behavior of semiconducting polymers. As a result, literature values for HOMO-LUMO gaps vary. For the purposes of this model, representative values were chosen and were implemented as rigid band gaps. The model also assumes atomically smooth interfaces, such as those achievable molecular beam epitaxy (MBE), between polymer layers. However, the interface between 2 polymer layers is more akin to the varied spacing between two stacked sets of spaghetti strands. Along some parts of the interface, polymer strands of different materials might touch whereas in other parts there might be a significant gap. A more rigorous molecular dynamics simulation might capture the consequences of fluctuations at the interface with greater accuracy.

Assuming 100% ideal photon-electron conversion efficiency is also experimentally inaccurate in that most conjugated polymers absorb a few percent of the incident spectrum along with significant exciton recombination losses.¹³ In this model, we only work with free charges. Exciton diffusion and polaron/bipolaron mechanisms of diffusion and dissociation are ignored. This assumption is possibly valid in the superlattice case since the donor acceptor interfaces are well within the exciton diffusion length of approximately 15nm. All excitons generated in the donor and acceptor layers will encounter a potential difference at a polymer interface with high probability and hence we can reasonably assume 100% conversion of excitons to free charges.

Furthermore, the model assumes coherent transport in that electron wavefunctions extend to the contacts in both directions. This allows for strong delocalization of charge carriers (large coherence lengths) when minibands are formed leading to large resonant tunneling currents. However, this assumption might not be valid in that most polymer semiconductors are not crystalline enough to allow such delocalization.

The most sensitive parameter in the model is the effective mass. At room temperature, the effective mass ratio between the well and barrier must be on the order of 5-10 to see significant miniband formation in bound states. In addition, strongest miniband formation is seen when the values of the effective masses are less than 1. A physical explanation for this sensitivity is not clear. Moreover, the idea of an effective mass itself is questionable when discussing organic systems. The effective mass approximation (EMA) assumes that the effect of periodic potential over the primitive cells in the crystal can be encompassed into a single quantity known as the effective mass. Given the effective mass, one can solve for the explicit form of the electron wavefunction considering only the potential in a single primitive cell.¹⁴ The EMA may not hold for conjugated polymers as they are not perfectly crystalline but rather have domains of crystallinity to various degrees. Hence, Bloch’s theorem, the essential ingredient in the EMA, is of questionably validity for conjugated polymers. Organic small molecules, on the other hand, might have enough crystallinity (particularly if deposited by Organic Molecular Beam Epitaxy

(OMBE)) to validate the coherent transport assumption and the EMA. However, in this study, we assume that the polymers are crystalline enough such that the EMA holds.

Experimental Work

Thin films of polypyrrole (PPy) were spin cast onto epitaxial GaAs at 5000rpm for 30s and 300 rpm for 45s with a 2000rpm/s ramp rate. Atomic Force Microscopy (AFM) measurements were taken to determine surface morphology and surface roughness of spin cast films. Figure 8 shows the result for a 0.01wt% PPy film.

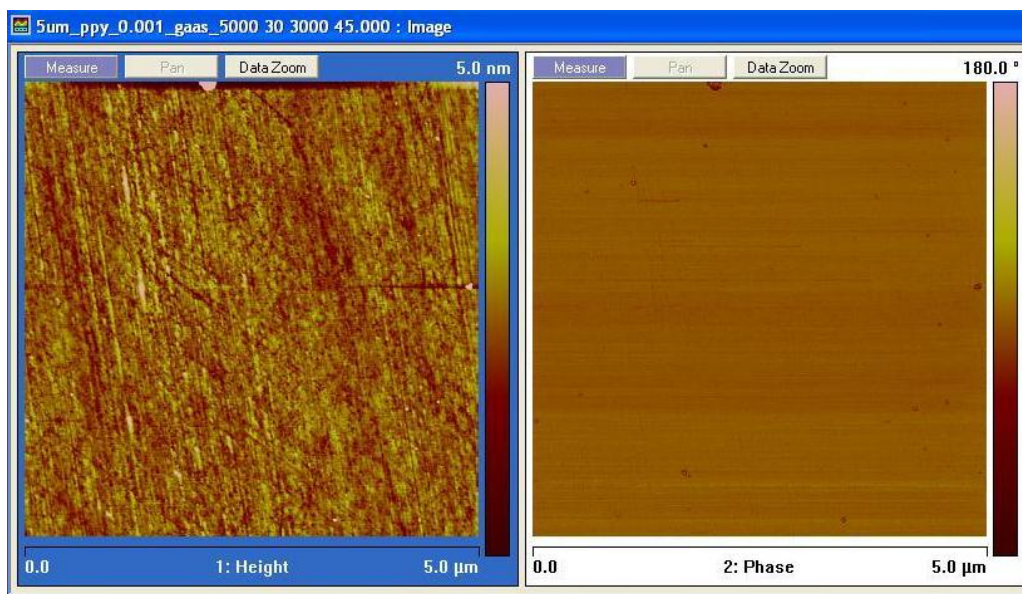


Figure 8: AFM for PPy 0.01wt% on GaAs

Next, spin casting recipes for ultrathin films were determined by measuring film thickness using Spectroscopic Ellipsometry (SE). Solutions of PPy and P3HT at 1wt%, 0.1wt%, and 0.01wt% were spin cast onto 100mm² square Si substrates at 5000rpm for 30s followed by 300rpm for 45s with a 2000rpm/s ramp rate. The 1wt% and 0.1wt% samples used a Kramer-Kronig consistent oscillator model to determine the optical constants and thickness. The 0.01wt% sample thicknesses were determined by fixing the optical constants from the 0.1wt% samples. The results are shown in Figure 9.

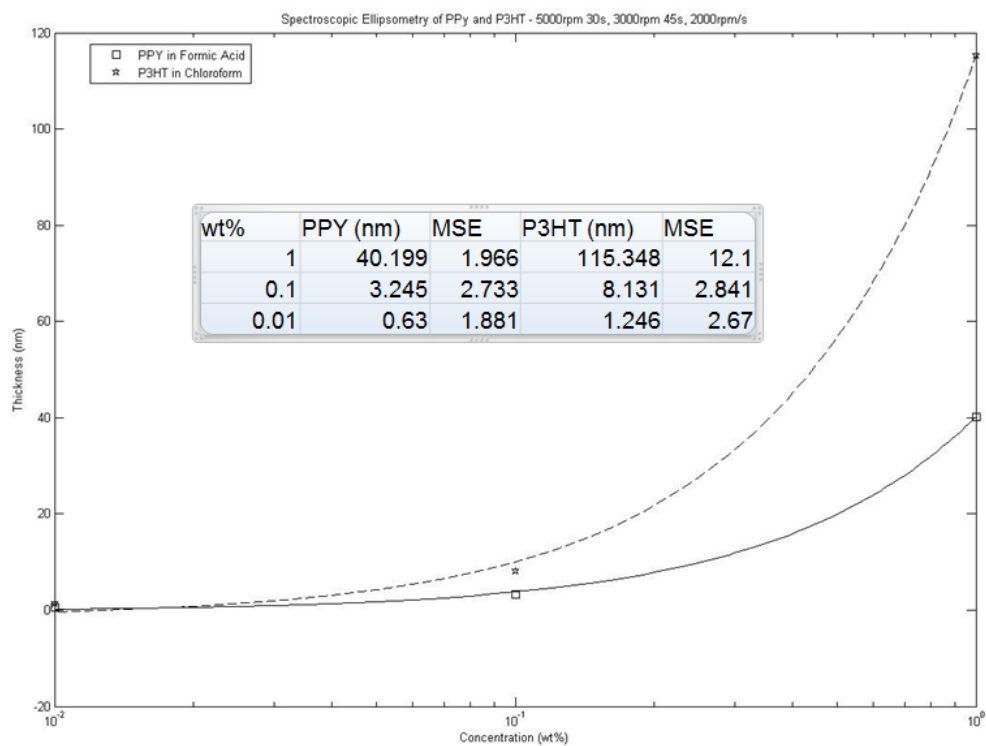


Figure 9: SE measurements of film thickness for PPy and P3HT

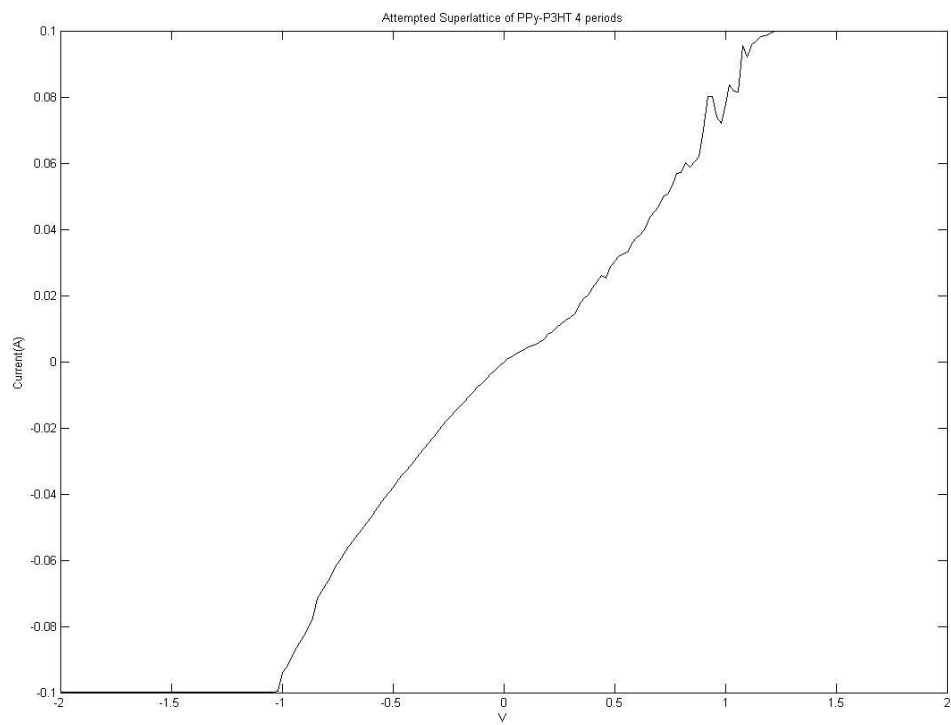


Figure 10: Attempted Superlattice of PPy and P3HT – 4 periods

Finally, a preliminary superlattice using 0.1 wt% PPy and 0.05 wt% P3HT was fabricated using high speed spin casting with the aforementioned procedure. The internal structure was not verified but rather only an I-V curve was measured and is shown in Figure 10.

Experimental Work Discussion

The RMS surface roughness of the PPy film was 0.4nm as measured by AFM. This value is close to the surface roughness on epitaxially smooth substrates indicating very smooth surfaces from high speed spin casting. There is not much contrast in the phase measurement and hence we can conclude that the polymer film is homogenous at the surface. However from the AFM measurement, it is difficult to predict whether the film is continuous or not, particularly since the concentration of the solutions used for spin casting were small. It is possible that a few monolayers were sparsely spread across the substrate and the average roughness of the polymer strands and large gaps with nothing on the substrate is a sub-nm value. Furthermore, it is not possible to determine the crystallinity or chain packing of such films with an AFM measurement. A small angle X-ray Diffraction technique (XRD) might be used to characterize the pseudo-crystalline polymer films. However, a foreseeable difficulty with XRD is that the signal from weakly crystalline domains might not be discernible from noise in the measurement.

The SE measurements show a linear relationship between the concentration of solution and film thickness (the x-axis in Figure 9 is log scale). For both polymers, PPy and P3HT, we conclude that films on the order of a few nanometers can be fabricated using concentrations in the 0.01-0.1 wt% range. Again, the SE measurements alone do not provide information about film continuity or crystallinity. Therefore, data from the AFM and SE measurements shows that it is possible to spin-cast <10nm films with sub-nm RMS surface roughness but does not provide any evidence of good crystallinity and chain packing, an essential requirement for observing resonant-tunneling behavior in a superlattice.

Finally, spin coating at high speeds can yield sub-nm surface roughness films but only works for immiscible polymer solutions thus severely restricting material choice. High speed spin coating can also break conjugation in polymer chains further diminishing the crystallinity of the material. Hence, an alternative solvent-free fabrication approach is Matrix-Assisted-Pulsed-Laser-Evaporation (MAPLE) where flash-frozen polymer targets are ablated under vacuum using a pulsed laser.

A preliminary conjugated polymer superlattice with 4 periods of PPy and P3HT was fabricated using spin casting at approximately 3nm per layer. The IV curve shows a weakly rectified behavior typical of a normal OPV (or IPV for that matter). There are some current fluctuations at approximately 1V. However, these fluctuations, potentially noise, cannot be firmly attributed to resonant tunneling as the internal structure of the superlattice was not characterized.

Furthermore, the degradation of the internal structure with repeated applications of bias is unknown. Contact dendriting, interface melding, and morphological degradation within each polymer layer can potentially contribute to errors in measurement. Consecutive measurements showed linear resistor-like IV behavior and hence indicate degradation in the device. It is interesting to note that even with the change in IV behavior over repeated voltage sweeps, the current fluctuation at approximately 1 V did not vanish. The cause for this is unknown.

Future Investigation

Further computational work may be performed by relaxing many of the strict assumptions of the model. A rigorous treatment of quantum transport will potentially be more accurate in modeling the true characteristics of a polymer superlattice device. Conjugated polymer-specific physics such as variation in chain packing, variation in energy band structure, exciton diffusion and recombination, polaron/bipolaron-mediated dissociation, and exciton-photon coupling and selection rules are potential topics of further study.

Experimentally, XRD can potentially be used to determine crystallinity of individual polymer layers and verify large scale periodicity across the superlattice. Cross-sectional Transmission Electron Microscopy (XTEM) can potentially be used to visually verify a superlattice structure although complications with contrast sensitivity might arise due to the similar densities of many conjugated polymers. Finally, once a superlattice has been fully characterized, a prototype device can be tested in a solar simulator to generate an illuminated IV and the data can be compared with the computational model.

Conclusions

In this study, the forward bias electrical transmission coefficient for an organic superlattice was modeled and used to compute the dark current and photocurrent versus applied bias. The total J-V characteristics for a MDMO-PPV:P3HT 4 period symmetric superlattice were computed and show a significantly larger maximum power output than that of a bilayer BHJ OPV. The model incorporated many strict assumptions that can be relaxed in future studies. However, under the assumptions listed, the model provides justification to pursue experimental investigation of superlattice nanostructures for OPVs. Preliminary fabrication of ultrathin films, characterized by AFM and SE, showed that high speed spin-casting of low concentration polymer solutions can yield <10nm thickness films with sub-nm RMS surface roughness. Degree of crystallinity and chain packing information is still a topic of future investigation.

Acknowledgements

I thank Prof. Adrienne D. Stiff-Roberts for her time and effort in guiding me to the completion of this work. I also thank Prof. Hisham Massoud, Prof. Steven Teitsworth, Kevin Lantz, Ryan Pate, and Ryan McCormick for illuminating discussions on device physics and for training me on

laboratory equipment. I thank Dean Martha Absher for the opportunity to participate in the Pratt Fellows Undergraduate Research Program.

References

- ¹<http://www.eia.doe.gov/oiaf/ieo/highlights.html>
- ²(2009). "Making Solar Energy Economical." from <http://www.engineeringchallenges.org/cms/8996/9082.aspx>. National Academy Engineering.
- ³(2008). Solar Energy Technologies Program Multi-Year Program Plan 2008-2012. DOE. Washington D.C., Office of Energy Efficiency and Renewable Energy.
- ⁴(2008). "NREL Solar Cell Sets World Efficiency Record at 40.8 Percent." from <http://www.nrel.gov/news/press/2008/625.html>.
- ⁵Gregg, B. and M. Hanna (2003). "Comparing organic to inorganic photovoltaic cells: Theory, experiment, and simulation." Journal of Applied Physics **93**(6).
- ⁶Yang, F. and S. Forrest (2008). "Photocurrent Generation in Nanostructured Organic Solar Cells." ACS-NANO **2**(5): 1022-1032.
- ⁷Benanti, T. and D. Venkataraman (2005). "Organic solar cells: An overview focusing on active layer morphology." Photosynthesis Research **87**: 73-81.
- ⁸Kim, J. Y., K. Lee, et al. (2007). "Efficient Tandem Polymer Solar Cells Fabricated by All-Solution Processing." Science **317**(222).
- ⁹<http://www.eia.doe.gov/cneaf/solar.renewables/page/trends/rentrends.html>
- ⁹ R. Tsu and L. Esaki, "Tunneling in a finite superlattice," *Appl. Phys. Lett.*, vol. 22, no. 11, pp. 562-564, 1973.
- ¹⁰Vatannia, S., Gildenblat, G (1996). "Airy's Functions Implementation of the Transfer-Matrix Method for Resonant Tunneling in variably Spaced Finite Superlattices." IEEE Journal of Quantum Electronics **32**(6).
- ¹¹Fromhold, A. T. J. (1981). Quantum Mechanics For Applied Physics and Engineering. New York, Academic Press.
- ¹²Giebink, N., Wiederrecht, G, Wasielewski, M, Forrest, S (2010). "Ideal Diode Equation for Organic Heterostructures. I. Derivation and Application." Physical Review B **82**.
- ¹³Sun, S.-S., Sariciftci, Niyazi (2005). Organic Photovoltaics - Mechanisms, Materials, and Devices. Boca Raton, CRC Press.
- ¹⁴Ashcroft, N., Mermin, D (1976). Solid State Physics. Orlando, Harcourt College Publishers.